1   **K18-hACE2 Mice for Studies of COVID-19 Treatments and Pathogenesis Including**

2   **Anosmia**

3   Jian Zheng[1#], Lok-Yin Roy Wong[1#], Kun Li[2#], Abhishek K. Verma[1], Miguel Ortiz[2], Christine

4   Wohlford-Lenane[2], Mariah R. Leidinger[3], C. Michael Knudson[3], David K. Meyerholz[3],

5   Paul B. McCray, Jr.[1,2]*, Stanley Perlman[1,2]*

6

7   [1]Departments of Microbiology and Immunology, [2]Pathology, and [3]Pediatrics, University

8   of Iowa, Iowa City, Iowa, USA

9

10   **Running title:** SARS-CoV-2 infection of K18-hACE2 mice

11   [#]Contributed equally to this manuscript

12   *Corresponding authors: Stanley Perlman, stanley-perlman@uiowa.edu

13   Paul B. McCray, Jr., paul-mccray@uiowa.edu

14   **Key words**: SARS-CoV-2, COVID-19, pathogenesis, convalescent plasma therapy,

15   anosmia.

16

17 **ABSTRACT**

18 The ongoing COVID-19 pandemic is associated with substantial morbidity and mortality.

19 While much has been learned in the first months of the pandemic, many features of

20 COVID-19 pathogenesis remain to be determined. For example, anosmia is a common

21 presentation and many patients with this finding show no or only minor respiratory signs.

22 Studies in animals experimentally infected with SARS-CoV-2, the cause of COVID-19,

23 provide opportunities to study aspects of the disease not easily investigated in human

24 patients. COVID-19 severity ranges from asymptomatic to lethal. Most experimental

25 infections provide insights into mild disease. Here, using K18-hACE2 mice that we

26 originally developed for SARS studies, we show that infection with SARS-CoV-2 causes

27 severe disease in the lung, and in some mice, the brain. Evidence of thrombosis and

28 vasculitis was detected in mice with severe pneumonia. Further, we show that infusion of

29 convalescent plasma (CP) from a recovered COVID-19 patient provided protection

30 against lethal disease. Mice developed anosmia at early times after infection. Notably,

31 while treatment with CP prevented significant clinical disease, it did not prevent anosmia.

32 Thus K18-hACE2 mice provide a useful model for studying the pathological

33 underpinnings of both mild and lethal COVID-19 and for assessing therapeutic

34 interventions.

35

36

37

38 **INTRODUCTION**

39 The COVID-19 pandemic is associated with more than 18 million cases and more than

40 650,000 deaths worldwide since its emergence in December of 2019. SARS-CoV-2 uses

41 the same receptor as SARS-CoV, human angiotensin-converting enzyme 2, (hACE2)[1].

42 Many of the animals infectable by SARS-CoV can also be experimentally infected with

43 SARS-CoV-2, but these animals generally develop mild disease[2-6]. Conversely, mice,

44 which are SARS-CoV-susceptible, are resistant to infection with SARS-CoV-2 because

45 of incompatibilities between mouse ACE2 and the viral spike protein[7]. Several

46 approaches have been or will be used to sensitize mice to infection, including providing

47 hACE2 by adenovirus transduction[8,9], mutating SARS-CoV-2 spike protein so that it binds

48 to mACE2[10], and modifying mACE2 so that cells are susceptible to SARS-CoV-2[11].

49 During the 2003-2004 SARS epidemic, since mice developed only mild disease, we and

50 others engineered mice that transgenically displayed hACE2[12-14]. K18-hACE2 mice

51 express hACE2 driven by cytokeratin 18 promoter, predominantly in epithelial cells[15].

52 SARS-CoV infected-K18-hACE2 mice developed an overwhelming encephalitis, with

53 lung disease characterized by aspiration pneumonia and evidence of mild virus-induced

54 pneumonia[12]. Both SARS-CoV-2 and SARS-CoV use hACE2 but show differences in

55 disease manifestations in patients. SARS-CoV-2 infects the upper airways to a much

56 greater extent than SARS-CoV and has been associated with clinical manifestations such

57 as anosmia, ageusia, thrombosis and endothelial damage in the lung vasculature, cardiac

58 and neurological disease, and a multisystem inflammatory disease in children and

59 adolescents[16-18]. Based on these observations, we reasoned that SARS-CoV-2 infection

60 of the K18-hACE2 mice might also show differences in pathogenesis. Here we

3

61 demonstrate the utility of K18-hACE2 mice for studies of COVID-19 disease and

62 treatments.

63

64 **RESULTS**

65 **K18-hACE2 transgenic mice develop significant disease following SARS-CoV-2**

66 **infection.**

67 To assess the susceptibility of K18-hACE2 mice to SARS-CoV-2, we performed an

68 intranasal challenge using inocula of 10^3, 10^4, and 10^5 PFU. As shown in Fig. 1a, we

69 observed a dose-dependent increase in weight loss and mortality. At the 10^5 PFU

70 inoculum, all animals succumbed, while there was variable mortality when mice were

71 inoculated with 10^4 PFU. To better understand the cause(s) of this morbidity and mortality,

72 we assessed the tissue distribution of viral genomic RNA by qRT PCR at 2, 4, and 6 days

73 post infection (dpi) in animals receiving the 10^5 PFU inoculum. The predominant target

74 organs were the lung at early timepoints, and variably, the brain at later timepoints (Fig.

75 1b, left panel). We also detected viral RNA in heart, liver, spleen, kidney, intestine, and

76 colon. To determine which tissues were sites of virus replication, we performed plaque

77 assays (Fig. 1b, right panel). The virus replicated to high titers in lung tissue at 2 dpi and

78 decreased at 4 and 6 dpi. In some, but not all animals, the brain tissue titers gradually

79 increased from 2 to 6 dpi. There was limited replication in the kidney, small intestine, and

80 colon, perhaps signifying low level hematogenous dissemination. We note that the K18

81 promoter predominantly directs gene expression to multiple epithelia-lined tissues[15].

82 While K18 is an epithelial cell protein, K18-based expression of a LacZ reporter was also

83 reported in cortical and brainstem neurons[19]. These results demonstrate that SARS-CoV-

4

84 2 infection of K18-hACE2 mice causes dose-dependent illness associated with significant

85 involvement of lungs with a subset of animals developing brain infection at higher inocula

86 (10^5 PFU).

87

88 **The SARS-CoV-2 pulmonary infection is extensive and progressive.**

89 In view of the early pulmonary virus replication, we stained lungs at 4 and 6 dpi for SARS-

90 CoV-2 antigen. Using an inoculum of 10^5 PFU, we observed extensive and diffuse

91 parenchymal localization of SARS-CoV-2 nucleocapsid (N) protein at 4 dpi that was less

92 intense by 6 dpi (Fig. 1c). Uninfected tissues showed no N protein signal. Examination of

93 hematoxylin and eosin stained tissues revealed extensive evidence of diffuse alveolar

94 damage with progressive alveolar/interstitial lesions characterized by edema,

95 inflammation, and focal cytomegaly in some alveolar lining cells (Fig. 1d). Also observed

96 was an accumulation of immune effector cells, including granulocytes and macrophages,

97 evidence of cell death, hemorrhage, hyaline membranes, occasional vascular thrombi,

98 and rare syncytia. Pulmonary vascular thrombi are often observed in severe human

99 COVID-19[16]. Between 4 and 6 dpi there was further progression of the findings of diffuse

100 alveolar damage. Alveolar septal thickening resulted from increased cellularity composed

101 of infiltrating inflammatory cells, dying cells with pyknotic to karyorrhectic nuclei, and a

102 proliferative alveolar epithelium with mitotic figures (Fig. 1d). These findings are further

103 summarized by histopathologic scoring at 4 and 6 dpi (Fig. 1e).

104

105 We also surveyed liver, heart, spleen, kidney, small intestine, and colon tissues for

106 disease associated changes (Extended Data Fig. 2). In the liver, we observed blood

107   vessels filled with aggregates composed of erythrocytes and platelets. At 4 dpi,

108   occasional vessels had evidence of fibrin thrombi adherent along the vascular wall

109   (Extended Data Fig. 2a), suggestive of the coagulopathy observed in COVID-19

110   autopsies [20]. The other tissues examined showed no disease-specific changes. To further

111   characterize the lung tissue responses to SARS-CoV-2 infection, we surveyed the

112   expression of several cytokines, chemokines, and innate immune transcripts at 2, 4, and

113   6 dpi by qRT PCR. As shown in Fig. 2a, there were significant increases in type I, II, and

114   III interferons, ISG-15, RIG-I, MDA5, IL-1β, IL-6, IL-8, IL-12, CCL-2, CCL-5, CCR7, CXCL-

115   2, CXCL-9, CXCL-10, and TNF compared to uninfected lungs over the course of infection.

116

Lung disease is characterized by an influx of immune effector cells

117

118   To further investigate the factors contributing to lung injury and virus clearance, we

119   performed immunophenotyping of infiltrating cells at 4 and 6 dpi. As shown in Fig. 2b-d,

120   we observed a progressive increase in the numbers of macrophages and monocytes,

121   neutrophils, and CD4 and CD8 T cells. Infiltrating inflammatory macrophage/monocytes

122   and neutrophils may have both protective and pathogenic roles, based on previous

123   studies of SARS and MERS[21]. Virus-specific T cells, which are required for optimal SARS-

124   CoV-2 clearance, were detected in lungs at 6 dpi. Virus-specific CD8 and CD4 T cells

125   responded to peptide pools representing SARS-CoV-2 S, N, and M proteins to varying

126   extents, as assessed by expression of IFN-γ and TNF respectively (Fig. 2b, c). Together

127   these results indicate that lung disease in K18-hACE2 mice shares features with severe

128   COVID-19. Another feature of severe human COVID-19 is an early antibody response,

6

129   consistent with plasmablast activation[22]. We detected serum neutralizing antibodies as

130   early as 6 dpi, consistent with such a response (Fig. 2e).

131

132   **SARS-CoV-2 causes brain infection in some K18-hACE2 mice.**

133   As shown in Fig. 1b, infectious virus was detected in the brains of most mice following

134   10^5 PFU intranasal inoculation. To investigate this in more detail, we immunostained

135   tissues for the viral N protein at 4 and 6 dpi. As shown in Fig. 3a, we observed no antigen

136   staining at 4 dpi (4/4 brains studied) but at 6 dpi saw extensive staining in several brain

137   regions including the olfactory bulb, cerebral cortex, caudate/putamen, thalamus,

138   hypothalamus, and ventral striatum (2/3 brains studied) (Extended Data Table 1).

139   Uninfected animals showed no N protein staining (3/3 animals studied). Many of these

140   areas are secondary or tertiary connections of the olfactory bulb, consistent with virus

141   entry at this site. H&E staining demonstrated cell death and thrombi in the thalamus (Fig.

142   3b, c) and neutrophilic and monocytic infiltrates in the meninges as well as cells

143   undergoing degeneration (Fig. 3d). The thalamus is affected in many COVID-19 patients

144   with neurological disease[23]. Of note, while most of the affected areas were connected to

145   the olfactory bulb, some, such as the area postrema and hypoglossal nucleus, are not

146   directly connected. Similar results were observed in analyses of SARS-CoV-infected

147   mice[24]. These results revealed an important role for olfactory bulb infection in spread to

148   the brain in some mice but also indicated that virus may enter the central nervous system

149   by other routes. Infection of the olfactory epithelium is expected to precede brain infection

150   and could also contribute to the anosmia and ageusia observed in many patients,

151   including some who are asymptomatic or mildly symptomatic.

7

152 **SARS-CoV-2 productively infects the sinonasal epithelium including sustentacular**

153 **cells.** To assess virus replication in the upper respiratory tract following intranasal

154 inoculation, we quantified viral RNA in nasal secretions by qRT PCR at 3 dpi. We

155 observed that secretions from 5 of 7 mice showed evidence of SARS-CoV-2 genomic

156 RNA (C_t =21.5 +/-1.2 (mean +/- SEM)), and of these 5, 4 had evidence of subgenomic

157 RNA (36.7 +/-1.1 (mean +/- SEM), consistent with active virus replication. Viral antigen

158 was readily detected in both the respiratory and olfactory epithelium at 2 and 5 dpi. At 2

159 dpi virus antigen was present at multiple sites, often at the interface of the olfactory and

160 respiratory epithelium (Fig. 3e). Viral antigen was also detected in nerve bundles

161 subjacent to the olfactory epithelium (Fig. 3f) and occasionally in vascular endothelia (Fig.

162 3g, left arrow) and Bowman's glands (Fig. 3g, right arrow). At sites of antigen positivity in

163 the olfactory epithelium and maxillary sinus, we observed cell death and cellular debris at

164 day 2 (Fig. 3h-j), which progressed to cell sloughing and loss of cellularity by 5 dpi. (Fig.

165 3k, l). ACE2 has been detected in sustentacular cells in the olfactory epithelium[25], but not

166 in olfactory sensory neurons, suggesting that these cells are a primary site of infection.

167 Consistent with this, we detected SARS-CoV-2 antigen in sustentacular cells (Fig. 3m-o).

168 Infection of sustentacular cells is not expected to result in spread to the olfactory bulb and

169 its connections, but could still contribute to anosmia.

170

171 **SARS-CoV-2 infected K-18-hACE2 mice exhibit anosmia**. To directly assess anosmia,

172 we performed two sets of behavioral tests, both of which require a normal sense of smell,

173 as described in Experimental Procedures. First, male mice were exposed to bedding

174 containing female or male dander in a 2 ml Eppendorf tube (Fig. 4a). Mice identify the

8

175 tube visually, and then preferentially spend time with the female dander, if olfaction is

176 normal. In a second experiment, we used a buried food test, in which mice are attracted

177 to a food item hidden in the bedding that they were previously conditioned to detect (Fig.

178 4c). K18-hACE2 mice infected with SARS-CoV-2 did worse than controls in both tests so

179 that at days 2 and 3 p.i., they spent less time in the vicinity of the female dander (Fig. 4b)

180 and took longer to find buried food (Fig. 4d, e). At 2 and 3 dpi, brains were not infected

181 (Fig. 1b). Additionally, mobility was largely normal since there were no differences in the

182 amount of time spent in exploring the tube containing male dander, when infected or

183 uninfected mice were compared (Fig. 4b). This suggests that anosmia at these times

184 points is primarily caused by infection of the nasal epithelium and is not a consequence

185 of spread to the brain.

186

187 **Human COVID-19 convalescent plasma protects mice from severe clinical disease**

188 **but not from anosmia.** Convalescent plasma (CP) from COVID-19 survivors is being

189 tested as a treatment in patients with clinical COVID-19[26]. Controlled studies are

190 underway but results of these studies have not yet been released. Studies have

191 demonstrated positive effects of CP on outcomes in several infectious diseases, if titers

192 are sufficiently high and if CP is administered early in the disease course[27]. To assess

193 the effect of CP on outcomes in K18-hACE2 mice infected with SARS-CoV-2, we

194 administered undiluted and diluted human high titer plasma (neutralizing titer 1:1,480) 12

195 hours before infection. Undiluted plasma administered 12 hours before infection protected

196 mice from death but not mild weight loss and reduced lung tissue titers while CP diluted

197 1:3 provided partial protection (Fig. 5a, c). Convalescent plasma pretreatment markedly

198   inhibited spread of infection to the brain (Fig. 5c). On examination of lung tissues, levels

199   of viral antigen and pathological changes were greatly decreased by CP treatment (Fig.

200   5d, e). Treatment did not seem to affect primary infection of lung cells but rather prevented

201   secondary spread within the lung. As shown in Fig. 5b, delivery of undiluted plasma at 24

202   hrs post infection (p.i.) demonstrated a partial protective effect. Finally, to assess the

203   effects of CP treatment on SARS-CoV-2-induced anosmia, we treated infected mice with

204   CP at 1 dpi and assessed mice for olfactory loss as described above (Fig. 4). Even though

205   mice had minimal signs of clinical disease after CP treatment, by day 4 all mice exhibited

206   profound anosmia (Fig. 4b, d, e).

207

208   **DISCUSSION**

209   When infected with SARS-CoV-2, K18-hACE2 mice developed a dose-dependent lung

210   disease phenotype with features similar to severe human COVID-19. This includes diffuse

211   alveolar damage, an influx of immune effector cells, tissue injury, lung vascular damage,

212   and death. Remarkably, the mice also support SARS-CoV-2 replication in the sinonasal

213   epithelium and associated with this pathology develop anosmia, a common feature of

214   human disease. Furthermore, the uniformly fatal disease outcome with a 10^5 inoculum

215   was prevented by pre-treatment with CP from a COVID-19 patient. Notably, CP pre-

216   treatment enhanced the kinetics of virus clearance but did not prevent initial infection of

217   the lungs, damage to nasal respiratory and olfactory epithelia, or anosmia. SARS-CoV-2

218   infection of K18-hACE2 mice treated with CP or, potentially, neutralizing monoclonal

219   antibodies will be especially useful for studies of anosmia because mice do not succumb

220   to the infection, but like many infected patients with mild disease, have olfactory loss as

10

221   a major manifestation[18]. Anosmia may result from damage to supporting sustentacular

222   cells and not to olfactory sensory neurons, suggesting that the resulting inflammatory

223   milieu, rather than direct neuronal damage is disease-causing. Therefore, we postulate

224   that the observed anosmia has at least two possible explanations. First, the infection of

225   sustentacular cells may disrupt signaling from olfactory sensory neurons (OSN) to the

226   olfactory bulb. For example, sustentacular cells provide support to OSN by maintaining

227   ion balance[28], which may be altered either directly by sustentacular cell infection or

228   indirectly via disorganization of the olfactory epithelium (OE), leading to loss of cilia from

229   OSN and deficient signal transduction[29]. The second possibility is collateral damage to

230   OSN resulting from pro-inflammatory cytokine secretion by SARS-CoV-2 infected

231   sustentacular cells. These cells have been reported to secrete cytokines such as TNF-α,

232   Il-1β, Il-1α, and CXCL2 in chronic rhinosinusitis and COVID-19 patients[30,31]. These are

233   not mutually exclusive explanations.

234

235   Although both SARS-CoV and SARS-CoV-2 use ACE2 to gain entry into cells and both

236   cause lung and brain disease, the disease manifestations are different. Most importantly,

237   SARS-CoV caused a brain infection when as little as 3.2 PFU were administered

238   intranasally[24], while even 10^4 PFU SARS-CoV-2 only variably infected the brain. A

239   consequence of this difference in CNS susceptibility is that lung damage was obvious

240   after SARS-CoV-2 infection, while it was obscured by the aspiration pneumonia that

241   developed in SARS mice as a consequence of probable infection of the cardio-respiratory

242   center in the medulla.

243

11

244   All K18-hACE2 mice succumbed to 10^5 SARS-CoV-2, from lung and, in some cases,

245   brain disease. This uniform lethality makes these mice useful for evaluation of anti-viral

246   therapies and vaccines, and also sets a high standard for their efficacy. This is illustrated

247   in Fig. 5, where mice treated with convalescent plasma were protected from lethal

248   disease, but not infection. This absence of complete protection could reflect use of human

249   convalescent plasma in mice, since some antibody effector functions are species-specific.

250   Of note, while most mice receiving 1:3 or 1:9 dilutions of convalescent plasma had no

251   evidence of brain infection (Fig. 5c), they succumbed to progressive lung disease.

252   Infection with a range of virus inocula will be useful for evaluation of therapeutic

253   interventions in a variety of pathological settings, as well as assessment of upper airway

254   disease and anosmia. Therefore, K18-hACE2 mice, readily available from Jackson

255   Laboratories, provide a useful model to study the pathogenesis of SARS-CoV-2-mediated

256   disease and to evaluate interventions.

257

258   **SUPPLEMENTAL INFORMATION** is linked to the online version of the paper.

259

260   **ACKNOWLEDGEMENTS**

266

AUTHOR CONTRIBUTIONS

Conceptualization and writing – original draft, P.B.M., S.P.; Data curation, A.K.V.; Formal analysis, J.Z., L-Y R.W., K.L., M.E.O., A.K.V., D.K.M., P.B.M., and S.P.; Investigation, J.Z., L-Y R.W., K.L., M.E.O., C.W-L, A.K.V., C.M.K., D.K.M., P.B.M., and S.P.; Visualization, A.K.V, M.R.L., D.K.M.; Resources, D.K.M., P.B.M., and S.P.; Writing – review and editing, J.Z., L-Y R.W., S.P. and P.B.M.

COMPETING FINANCIAL INTERESTS

The authors declare no competing financial interests.

REFERENCES

1   Zhou, P. *et al.* A pneumonia outbreak associated with a new coronavirus of probable bat origin. *Nature* **579**, 270-273, doi:10.1038/s41586-020-2012-7 (2020).
2   Chan, J. F. *et al.* Simulation of the clinical and pathological manifestations of Coronavirus Disease 2019 (COVID-19) in golden Syrian hamster model: implications for disease pathogenesis and transmissibility. *Clin Infect Dis*, doi:10.1093/cid/ciaa325 (2020).
3   Munster, V. J. *et al.* Respiratory disease and virus shedding in rhesus macaques inoculated with SARS-CoV-2. *bioRxiv*, doi:10.1101/2020.03.21.001628 (2020).
4   Rockx, B. *et al.* Comparative pathogenesis of COVID-19, MERS, and SARS in a nonhuman primate model. *Science* **368**, 1012-1015, doi:10.1126/science.abb7314 (2020).
5   Shi, J. *et al.* Susceptibility of ferrets, cats, dogs, and other domesticated animals to SARS-coronavirus 2. *Science* **368**, 1016-1020, doi:10.1126/science.abb7015 (2020).
6   Sia, S. F. *et al.* Pathogenesis and transmission of SARS-CoV-2 in golden hamsters. *Nature* **583**, 834-838, doi:10.1038/s41586-020-2342-5 (2020).
7   Wan, Y., Shang, J., Graham, R., Baric, R. S. & Li, F. Receptor Recognition by the Novel Coronavirus from Wuhan: an Analysis Based on Decade-Long Structural Studies of SARS Coronavirus. *J Virol* **94**, doi:10.1128/JVI.00127-20 (2020).
8   Hassan, A. O. *et al.* A SARS-CoV-2 Infection Model in Mice Demonstrates Protection by Neutralizing Antibodies. *Cell*, doi:10.1016/j.cell.2020.06.011 (2020).
9   Sun, J. *et al.* Generation of a Broadly Useful Model for COVID-19 Pathogenesis, Vaccination, and Treatment. *Cell*, doi:10.1016/j.cell.2020.06.010 (2020).
10   Dinnon, K. H. *et al.* A mouse-adapted SARS-CoV-2 model for the evaluation of COVID-19 medical countermeasures. *bioRxiv*, doi:10.1101/2020.05.06.081497 (2020).

300 11   Sun, S. H. *et al.* A Mouse Model of SARS-CoV-2 Infection and Pathogenesis. *Cell Host*
301   *Microbe* **28**, 124-133 e124, doi:10.1016/j.chom.2020.05.020 (2020).
302 12   McCray, P. B., Jr. *et al.* Lethal infection in K18-hACE2 mice infected with SARS-CoV. *J Virol*
303   **81**, 813-821 (2006).
304 13   Tseng, C. T. *et al.* SARS coronavirus infection of mice transgenic for the human
305   angiotensin-converting enzyme 2 (hACE2) virus receptor. *J Virol* **81**, 1162-1173 (2006).
306 14   Yang, X. H. *et al.* Mice transgenic for human angiotensin-converting enzyme 2 provide a
307   model for SARS coronavirus infection. *Comp Med* **57**, 450-459 (2007).
308 15   Chow, Y. H. *et al.* Development of an epithelium-specific expression cassette with human
309   DNA regulatory elements for transgene expression in lung airways. *Proc Natl Acad Sci U S*
310   *A* **94**, 14695-14700 (1997).
311 16   Ackermann, M. *et al.* Pulmonary Vascular Endothelialitis, Thrombosis, and Angiogenesis
312   in Covid-19. *N Engl J Med* **383**, 120-128, doi:10.1056/NEJMoa2015432 (2020).
313 17   Feldstein, L. R. *et al.* Multisystem Inflammatory Syndrome in U.S. Children and
314   Adolescents. *N Engl J Med* **383**, 334-346, doi:10.1056/NEJMoa2021680 (2020).
315 18   Spinato, G. *et al.* Alterations in Smell or Taste in Mildly Symptomatic Outpatients With
316   SARS-CoV-2 Infection. *JAMA*, doi:10.1001/jama.2020.6771 (2020).
317 19   Chow, Y. H. *et al.* Targeting transgene expression to airway epithelia and submucosal
318   glands, prominent sites of human CFTR expression. *Mol Ther* **2**, 359-367,
319   doi:10.1006/mthe.2000.0135 (2000).
320 20   Bradley, B. T. *et al.* Histopathology and ultrastructural findings of fatal COVID-19
321   infections in Washington State: a case series. *Lancet* **396**, 320-332, doi:10.1016/S0140-
322   6736(20)31305-2 (2020).
323 21   Channappanavar, R. *et al.* Dysregulated type I interferon and inflammatory monocyte-
324   macrophage responses cause lethal pneumonia in SARS-CoV-infected mice. *Cell Host*
325   *Microbe* **19**, 181-193, doi:10.1016/j.chom.2016.01.007 (2016).
326 22   Mathew, D. *et al.* Deep immune profiling of COVID-19 patients reveals distinct
327   immunotypes with therapeutic implications. *Science*, doi:10.1126/science.abc8511
328   (2020).
329 23   Poyiadji, N. *et al.* COVID-19-associated Acute Hemorrhagic Necrotizing Encephalopathy:
330   Imaging Features. *Radiology* **296**, E119-E120, doi:10.1148/radiol.2020201187 (2020).
331 24   Netland, J., Meyerholz, D. K., Moore, S., Cassell, M. & Perlman, S. Severe acute respiratory
332   syndrome coronavirus infection causes neuronal death in the absence of encephalitis in
333   mice transgenic for human ACE2. *J Virol* **82**, 7264-7275 (2008).
334 25   Bilinska, K., Jakubowska, P., Von Bartheld, C. S. & Butowt, R. Expression of the SARS-CoV-
335   2 Entry Proteins, ACE2 and TMPRSS2, in Cells of the Olfactory Epithelium: Identification
336   of Cell Types and Trends with Age. *ACS Chem Neurosci* **11**, 1555-1562,
337   doi:10.1021/acschemneuro.0c00210 (2020).
338 26   Joyner, M. J. *et al.* Early safety indicators of COVID-19 convalescent plasma in 5,000
339   patients. *J Clin Invest*, doi:10.1172/JCI140200 (2020).
340 27   Casadevall, A., Joyner, M. J. & Pirofski, L. A. SARS-CoV-2 viral load and antibody responses:
341   the case for convalescent plasma therapy. *J Clin Invest*, doi:10.1172/JCI139760 (2020).

342 28 Vogalis, F., Hegg, C. C. & Lucero, M. T. Ionic conductances in sustentacular cells of the
343   mouse olfactory epithelium. *J Physiol* **562**, 785-799, doi:10.1113/jphysiol.2004.079228
344   (2005).
345 29 Bryche, B. *et al.* Massive transient damage of the olfactory epithelium associated with
346   infection of sustentacular cells by SARS-CoV-2 in golden Syrian hamsters. *Brain Behav*
347   *Immun*, doi:10.1016/j.bbi.2020.06.032 (2020).
348 30 Imamura, F. & Hasegawa-Ishii, S. Environmental Toxicants-Induced Immune Responses in
349   the Olfactory Mucosa. *Front Immunol* **7**, 475, doi:10.3389/fimmu.2016.00475 (2016).
350 31 Torabi, A. *et al.* Proinflammatory Cytokines in the Olfactory Mucosa Result in COVID-19
351   Induced   Anosmia.   *ACS   Chem   Neurosci*   **11**,   1909-1913,
352   doi:10.1021/acschemneuro.0c00249 (2020).
353 32 Meyerholz, D. K. & Beck, A. P. Fundamental Concepts for Semiquantitative Tissue Scoring
354   in Translational Research. *ILAR J* **59**, 13-17, doi:10.1093/ilar/ily025 (2018).
355 33 Li, K. *et al.* Middle East Respiratory Syndrome Coronavirus Causes Multiple Organ Damage
356   and Lethal Disease in Mice Transgenic for Human Dipeptidyl Peptidase 4. *J Infect Dis* **213**,
357   712-722, doi:10.1093/infdis/jiv499 (2016).
358 34 Yang, M. & Crawley, J. N. Simple behavioral assessment of mouse olfaction. *Curr Protoc*
359   *Neurosci* **Chapter 8**, Unit 8 24, doi:10.1002/0471142301.ns0824s48 (2009).

360
361
362
363
364

365

366

367

368 **EXPERIMENTAL PROCEDURES**

369 **Human subjects approval.**

370 Written informed consent was obtained from subjects to obtain plasma for participation in

371 this study. The study was approved by the Institutional Review Board of the University of

372 Iowa (IRB (#202003554 and #201402735).

373

374 **Mice, cells, and virus.**

375 Transgenic mice expressing human ACE2 were previously reported [12]. Human ACE2 is

376 expressed under control of the cytokeratin 18 promoter. The mice used in these studies

377 were obtained from the Jackson Laboratory (034860-B6.Cg-Tg(K18-ACE2)2Prlman/J)

378 and are congenic on the C57BL/6 background. Non-transgenic C57BL/6 mice were used

379 as controls in some experiments.

380 All protocols were approved by the Institutional Animal Care and Use Committees of the

381 University of Iowa. The 2019n-CoV/USA-WA1/2019 strain of SARS-CoV-2 (Accession

382 number: MT985325.1) used in these studies was passaged on Calu-3 2B4 cells. Calu-3

383 2B4 cells were grown in MEM (GIBCO, Grand Island, NY) supplemented with 20% FBS.

384 Vero E6 cells were grown in Dulbecco's modified Eagle's medium (DMEM, GIBCO, Grand

385 Island, NY) supplemented with 10% fetal bovine serum (FBS).

386

387 **Infection of mice.**

388 Mice were lightly anesthetized with ketamine/xylazine and infected intranasally with the

389 indicated amount of SARS-CoV-2 in a total volume of 50 µl DMEM. Animal weight and

16

390 health were monitored daily. All experiments with SARS-CoV-2 were performed in a

391 Biosafety Level 3 (BSL3) Laboratory at the University of Iowa.

392

393 **Nasal lavage**. Mice were sedated with ketamine/xylazine (100 mg/kg ketamine/12.5

394 mg/kg xylazine). 100 µl of Carbachol (100 µg/ml) was administered I.P. and after

395 approximately 15 minutes, nasal secretions were recovered. 20 µl secretions were

396 recovered per mouse. Nasal secretions were immediately added to 500 µl Trizol, mixed

397 and stored at -80°C until RNA was isolated.

398

399 **Virus titer by plaque assay.**

400 Virus or tissue homogenate supernatants were serially diluted in DMEM. 12 well plates

401 of VeroE6 cells were inoculated at 37°C in 5% CO_2 for 1 h and gently rocked every 15

402 min. After removing the inocula, plates were overlaid with 1.2% agarose containing 4%

403 FBS. After 3 days, overlays were removed, and plaques visualized by staining with 0.1%

404 crystal violet. Viral titers were quantified as PFU/mL tissue.

405

406 **Flow Cytometry.**

407 The following monoclonal antibodies were used: anti-mouse CD3e-BV421 (clone 145-

408 2C11, Cat. No.: 562600), anti-mouse CD16/32 (clone 93, Cat. No.:101302), anti-mouse

409 CD4-PercP (clone RM4-5, Cat. No.: 550954), anti-mouse CD8-APC-Cy7 (clone 53-6.7,

410 Cat. No.: 100714), anti-mouse CD220-APC (clone RA3-6B2, Cat. No.: 553092), anti-

411 mouse Ly6C-PerCP (clone HK1.4, Cat. No.: 128028), anti-mouse Ly6G-FITC (clone 1A8,

412 Cat. No.: 127606), anti-mouse CD11b-BV510 (clone M1/70, Cat. No.: 101263), anti-

413   mouse CD11c-BV421 (clone N418, Cat. No.: 117343), anti-mouse CD64-PE-Cy7 (X54-

414   5/7.1), Biolegend, San Diego, CA; anti-mouse CD103-APC (clone 2E7, Cat. No.: 17-

415   1031-80), anti-mouse TNF-FITC (clone MP6-XT22, Cat. No.: 11-7321-82), anti-mouse

416   IFN-γ-APC (clone XMG1.2, Cat. No.: 25-7311-82), eBioscience, San Diego, CA; and

417   mouse anti-C9 antibody (clone Rho 1D4, Cat. No.: MAB5356, EMD Millipore). For

418   intracellular cytokine staining (ICS), lymphocytes were cultured in 96-well dishes at 37°C

419   for 5-6 h in the presence of 2 μM peptide pool and brefeldin A (BD Biosciences). Cells

420   were then labeled for cell-surface markers, fixed/permeabilized with Cytofix/Cytoperm

421   Solution (BD Biosciences), and labeled with anti-IFN-γ and anti-TNF antibody. All flow

422   cytometry data were acquired using a BD FACSVerse and analyzed with FlowJo

423   software.

424

425   **Histology and Immunohistochemistry.**

426   Animals were anesthetized and perfused transcardially with PBS, followed by zinc

427   formalin. Lungs were fixed in zinc formalin. For routine histology, tissue sections (~4 μm

428   each) were stained with hematoxylin and eosin. The following criteria were used for

429   scoring edema, hyaline membrane formation and necrotic cellular debris: 0- none; 1-

430   uncommon detection in <5% lung fields (200x); 2- detectable in up to 33% of lung fields;

431   3- detectable in up to 33-66% of lung fields; 4- detectable in >66% of lung fields. For

432   scoring neutrophil infiltration: 0- within normal limits; 1-scattered PMNs sequestered in

433   septa; 2- #1 plus solitary PMNs extravasated in airspaces; 3-#2 plus small aggregates in

434   vessel and airspaces. For scoring mononuclear infiltrates, thrombosis and hemorrhage:

435   0-none; 1 - uncommon detection in <5% lung fields (200x); 2- detectable in up to 33% of

18

436   lung fields; 3- detectable in up to 33-66% of lung fields; 4- detectable in >66% of lung

437   fields.

438   For SARS-CoV-2 antigen detection, slides were incubated with blocking reagent (10%

439   normal goat serum x 30 minutes) followed by rabbit monoclonal antibody against SARS-

440   CoV2 N protein (1:20,000 dilution x 60 minutes, #40143-R019, Sino Biological US Inc.,

441   Wayne, PA, USA), then incubated with Rabbit Envision (Dako) and diaminobenzidine

442   (Dako) as chromogen. Tissues were examined and scored in a post-examination method

443   of masking by a boarded experimental pathologist [32]. Ordinal scores for lesion parameters

444   were assigned using the following tiers: 0 = within expected limits; 1 - uncommon, <5%;

445   2 - detectable in 5-33%; 3 - detectable in 34-66% and 4 - detectable in >66% of lung fields

446   (200x objective magnification).

447

448   **Human convalescent plasma.**

449   High titer convalescent plasma was collected with subject consent under an IRB

450   (#202003554) approved protocol that allows use of samples for research.   The

451   convalescent plasma donor was a 58 year old female who had molecularly confirmed

452   COVID-19 more than 4 weeks prior to their donation. Following the donation, she tested

453   positive for HLA antibodies so the plasma was not eligible for administration to patients

454   and was diverted to research.   Antibody testing (EUROIMMUN SARS-COV-2 ELISA

455   (IgG)) performed on this donor was 9.8, well above the cutoff of 1.1 for a positive result.

456   Neutralization titer using a luciferase-expressing SARS-CoV-2 S protein pseudovirus

457   assay showed that the neutralization IC_{50} titer was 1:1,480. Control plasma was obtained

458   from an expired plasma unit collected prior to COVID-19 spread in our area and this

459   product was collected under an IRB (#201402735) approved protocol that allows for

460   research use of these products.

461

RNA isolation and qRT PCR.

463   Total RNA was extracted from tissues (or nasal lavage) using Trizol (Invitrogen)

464   according to the manufacturer's protocol. Following a DNase treatment step 200 ng of

465   total RNA was used as a template for first strand cDNA. The resulting cDNA was

466   subjected to amplification of selected genes by real-time quantitative PCR using Power

467   SYBR Green PCR Master Mix (Applied Biosystems). Average values from duplicates of

468   each gene were used to calculate the relative abundance of transcripts normalized to

469   HPRT and presented as $2^{-\Delta CT}$. The primers used for cytokine and chemokines were

470   previously reported[33]. For detection of viral genomes, the following primers were used to

471   amplify the genomic RNA for the N protein: 2019-nCoV_N1-F: 5'-GAC CCC AAA ATC

472   AGC GAA AT-3'; 2019-nCoV_N1-R: 5'-TCT GGT TAC TGC CAG TTG AAT CTG-3'.

473   The following primers were used to amplify the subgenomic RNA for the E protein: F: 5'-

474   CGATCTCTTGTAGATCTGTTCTC-3'; R: 5'-ATATTGCAGCAGTACGCACACA-3'.

475

Pseudovirus neutralizing antibody assay: To determine neutralization activity of

477   patient and mouse plasma, we used a luciferase reporter-based pseudovirus

478   neutralization assay, which has a nonreplicative vesicular stomatitis virus backbone

479   coated with the SARS-CoV-2 spike protein. Sera from SARS-CoV-2-infected K18-

480   hACE2 mice were collected at the indicated time points and heat inactivated by

481   incubation at 56°C for 30 min. Human convalescent plasma or mouse sera were serially

482   diluted twofold in 96-well plates and incubated with the same volume of VSV

483   pseudotyped with SARS-CoV-2 spike protein at 37°C for 1 h. Samples were placed onto

484   Vero E6 cells and incubated at 37°C for 1 h to allow virus binding. After removal of the

485   initial inoculum, cells were incubated for 24 hours. Neutralization was measured with a

486   luciferase assay kit (Promega) and plotted relative to the value for control wells.

487

488   **Behavioral studies.**

489   ***Social Scent Discrimination Test***. Social-scent discrimination task was designed to

490   assess the capability of mice to discriminate social scents as described previously [34]. Two

491   identical tubes were separately sealed in a Ziploc bag in a large cage (used for housing

492   rats (31 cm x 26 cm x 22 cm)) containing bedding from female mice and from the

493   experimental cage overnight. Next, mice were released in a fresh cage containing the

494   tubes placed at two different corners. Sniffing latency (sniffing and exploring the tubes)

495   was calculated within a 5 min period. One trial on each mouse was performed each day

496   with the position of tubes changed daily. Data were recorded in the BSL3 facility from a

497   distance of approximately 1 meter.

498   ***Buried Food Test***: Evaluation of odor detection was carried out by a buried food test (bft)

499   as described previously[34]. Briefly, food was confirmed prior to initiation of the

500   experiments. Mice were sensitized to the food for 10-15 minutes on the day of the

501   experiment. The food pellet was then buried approximately 1 cm below the surface of

502   bedding in a fresh cage. One trial per mouse per day was performed with a changed

503   position of food on a daily basis. The latency to locate and uncover the buried food pellet

504   was recorded with a stopwatch. Mice were allowed to explore the cage for 4 min and if

505   they could not locate the food, the time was recorded as 4 min. The experiment was

506   repeated daily.

Statistical analysis.

508   ANOVA and Student's t tests were used to analyze differences in mean values between

509   groups using GraphPad Prism 7. All results are expressed as mean ± standard error

510   (SEM) and were corrected for multiple comparisons. For behavioral studies, data from

511   the social scent discrimination test, and buried food test were analyzed by two-way

512   ANOVA and one-way ANOVA tests, respectively. *P* values of <0.05 were considered

513   statistically significant. (*, *P values of ≤0.05. **, P values of ≤0.005. ***, P values of*

514   *≤0.0005. ****, P values of ≤0.0001).*

515

Data availability.

517   The data supporting the findings of this study are documented within the paper and are

518   available from the corresponding authors upon request.

519

520

521

22

522 **FIGURE LEGENDS**

523 **Fig. 1. Clinical and pathological disease in K18-hACE2 transgenic mice following**

524 **SARS-CoV-2 infection**. a. Percentage of initial weight and survival of K18-hACE2 mice

525 infected with 10^3, 10^4, and 10^5 PFU SARS-CoV-2/mouse. b. Viral RNA detected by qPCR

526 targeting viral N gene with normalization to HPRT for the indicated organs at 2, 4, and 6

527 dpi (left panel). Infectious virus titers detected by plaque assay in different organs at 2, 4,

528 and 6 dpi (right panel). LOD=limit of detection. c. Lungs from uninfected (n=3), and

529 infected (day 4 (n=4) and day 6 (n=3) p.i.) were analyzed by immunohistochemistry using

530 anti-SARS-CoV-2 N antibody. d. Sections of paraffin-embedded lungs were stained with

531 H&E. Note airway edema and alveolar hyaline membranes (asterisks, middle bottom

532 panel), vascular thrombosis (inset, top right, 6 dpi 20x panel), dying cells with pyknotic to

533 karyorrhectic nuclei, and a proliferative alveolar epithelium with mitotic figures (arrowhead

534 and inset, lower right, 6 dpi 20x panel). e. Summary of histological scoring in the lungs,

535 as described in Experimental Procedures.

536

537 **Fig. 2. Inflammatory mediators and immune effector cells contribute to lung**

538 **disease phenotype**. a. Cytokine and chemokine transcripts were measured by qPCR

539 following reverse transcription of RNA isolated from the lungs of SARS-CoV-2 infected

540 K18-hACE2 mice (n=3 or 4 for each time point). Statistical significance compared to

541 results obtained at 0 dpi. b. Representative FACS plot of IFNγ+TNF+ CD8 and CD4 T

542 cells after stimulated with indicated peptide pools) in the lungs of 10^5 PFU SARS-CoV-2

543 infected K18-hACE2 mice. c. Summary data are shown (n=3 mice/time point). d.

544 Quantification of immune cells in the lungs (n=3 for uninfected group and n=4 for 4 and 6

545   dpi). e. Sera were collected from infected mice at the indicated time points and IC_{50} values

546   determined by neutralization of SARS-CoV-2 pseudoviruses expressing luciferase.

547

548   **Fig. 3. Some K18-hACE2 mice develop brain disease after SARS-CoV-2 infection**.

549   a. Brains were prepared from uninfected and infected mice and analyzed for SARS-CoV-

550   2 by immunohistochemistry. b, c. Multiple sites of dead cells (arrows) characterized by

551   cellular and karyorrhectic nuclear debris (b, arrows) and of thrombi (c, arrow and inset) in

552   thalamus. Bar = 17 μm. d. Examination of meninges at day 6 p.i. revealed increased

553   cellularity composed of degenerate cells and neutrophils and mononuclear cells. Cellular

554   and karyorrhectic nuclei debris were also detected in the perivascular regions (200X). e-

555   o. Nasal and sinus tissue were examined at days 2 (e-j) and 5 (k-o) p.i. e-h. Olfactory

556   epithelium (OE) was stained with anti-SARS-CoV-2 N antibody (e-g) or H&E stain (h). f.

557   Nerve bundles (NB) subjacent to OE had punctate immunostaining (brown, arrows). g.

558   Subjacent to sites of immunostaining for N protein (brown, black arrows), endothelial

559   lining of vessels (left arrow) and bowman glands (right arrow) were occasionally positive

560   for virus antigen (brown). h. Sites of N protein localization in OE had evidenced of cell

561   death and cellular debris (arrows). Bar = 100 μm (e) and 25 μm (f-h). i-j. Maxillary sinus

562   (MS) stained with anti-SARS-CoV-2 N antibody (i) or H&E (j). i. MS lining epithelium had

563   extensive immunostaining for N protein (brown, arrows). j. ME epithelium had common

564   sloughing and cellular debris (arrowheads). The lateral nasal glands (LNG) also had

565   multifocal cellular and karyorrhectic debris (arrows). Bar = 75 μm (i) and 19 μm (j),

566   respectively. k-l. Olfactory epithelium still had foci of SARS-CoV-2 N protein

567   immunostaining at d. 5 p.i. (k, arrows, left) that was often localized near interface with

24

568 respiratory epithelium. In these sites, there was cellular sloughing and loss of cellularity

569 (arrows, right). 200x. m-o. Arrows point to "classic" morphology and strong labeling of

570 sustentacular cells with expanding labeling of adjacent cells. Bar = 50 (m) and 25 μm (n,

571 o).

572

573 **Fig. 4. SARS-CoV-2 infection causes anosmia in K18-hACE2 mice**.

574 a. Schematic showing social scent discrimination test. b. Each male mouse was allowed

575 5 minutes in the cage with male and female scent (bedding from male or female cages)

576 placed at two corners of the cage. The time that male mice spent sniffing male or female

577 scent was recorded. Data were analyzed by 2-way ANOVA. ***p<0.001. In some

578 experiments, mice were pretreated with undiluted convalescent plasma (results on right

579 of vertical line). c. Schematic showing buried food test. d. Buried food test. Food was

580 buried under the bedding and each mouse was allowed 4 minutes in the cage to search

581 for the food. The dotted line shows the time limit of 4 minutes. Data were analyzed by 1-

582 way ANOVA. ****p<0.0001. e. The percentage of mice that found the buried food within

583 4 minutes is shown. In some experiments, mice were pretreated with undiluted

584 convalescent plasma (denoted by blue bars in d, e).

585

586 **Fig. 5. Effects of convalescent plasma on outcomes in SARS-CoV-2-infected K18-**

587 **hACE2 mice.** a. Percentage of initial weight (left panel) and survival (right panel) of

588 infected K18-hACE2 mice receiving control serum (n=4, black), undiluted (n=4, blue), 1:3

589 diluted (n=4, red) and 1:9 diluted (n=3, purple) human convalescent plasma at 24 hours

590 prior to challenge of 10^5 PFU SARS-CoV-2. b. Percentage of initial weight (left panel),

25

591   and survival (right panel) of K18-hACE2 mice receiving control plasma (n=2) or undiluted

592   CP (n=4) at 24 hours after challenge with 10^5 PFU SARS-CoV-2. c. Viral titers of CP-

593   treated mice in the lungs (left panel) and brains (right panel) at 2 and 5 dpi. LOD=limit of

594   detection. d. Scoring for N protein abundance in CP-treated mice in the nasal cavity at 2

595   (left panel) and 5 (right panel) dpi. 0 – none; 1 - rare <1%; 2 - multifocal or localized <33%

596   cells; 3 - multifocal, coalescing, 33-66%; 4 - extensive >67%. e. N protein staining in the

597   lungs of control or convalescent plasma treated mice at 2 and 5 days p.i. Bar = 370 µm

598   (top) and 75 µm (bottom).

599

600   **Extended Data Fig. 1. Histological analysis of extrapulmonary tissue in SARS-CoV-**

601   **2-infected K18-hACE2 mice.** Mice were sacrificed at days 0, 4 and 6 p.i. and tissues

602   prepared for histological examination (n=3/4 per group). Liver (a), spleen (b), kidney (c),

603   small intestine (d), and colon (e) were studied. Pathological changes were minor and only

604   observed in the liver. In the liver, all mice had some blood vessels filled with clear space

605   or aggregates variably composed of erythrocytes / platelets (insets). Rare vessels had

606   evidence of eosinophilic fibrillar material consistent with fibrin thrombi (arrows, inset in

607   middle panel) adherent along the vascular wall.

608

609   **Extended Data Fig. 2**. Gating strategy for identification of immune cells in lungs is shown.
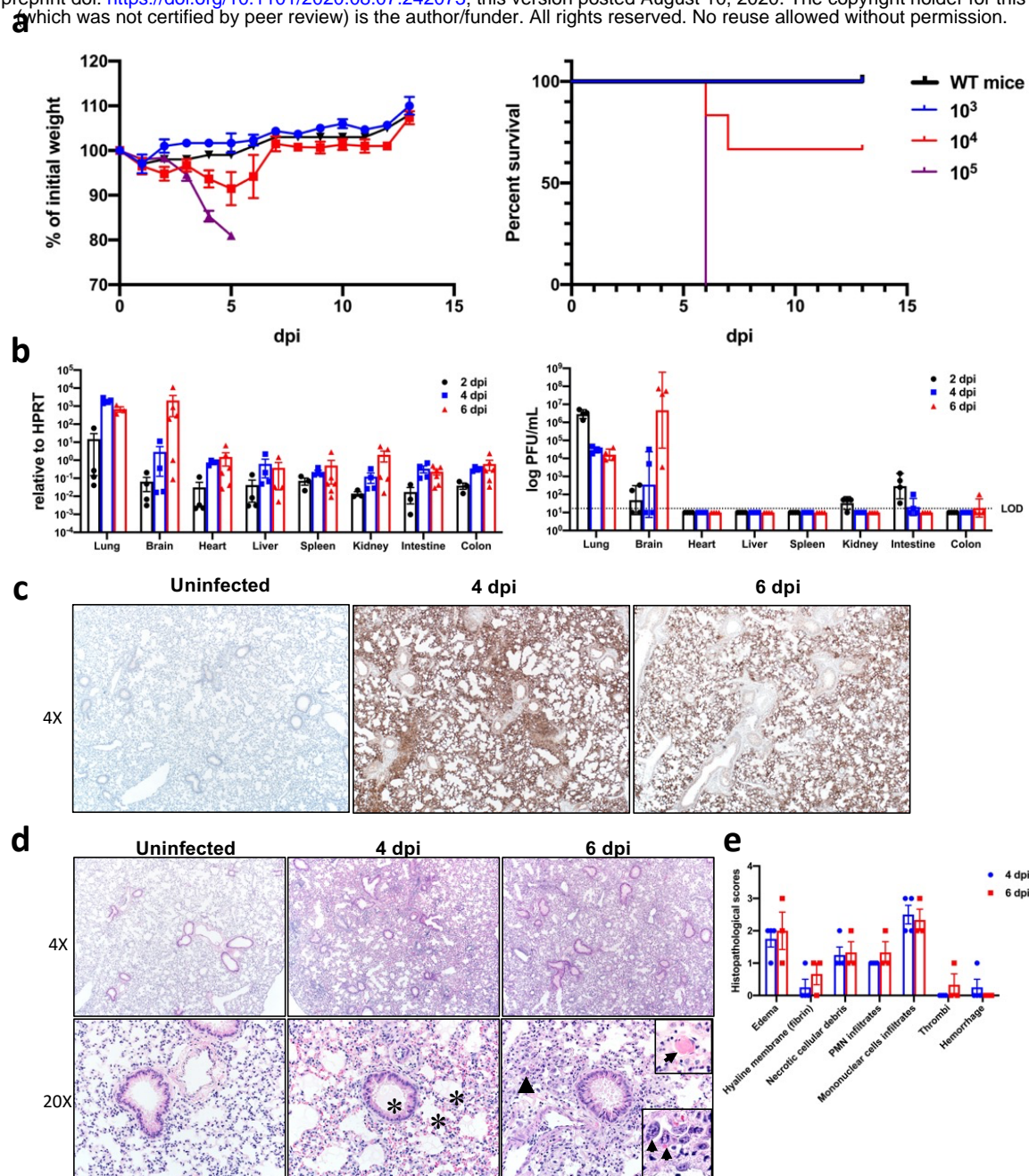
610
611
612

Figure 1

Fig. 1. Clinical and pathological disease in K18-hACE2 transgenic mice following SARS-CoV-2 infection. a. Percentage of initial weight and survival of K18-hACE2 mice infected with 10^3, 10^4, and 10^5 PFU SARS-CoV-2/mouse. b. Viral RNA detected by qPCR targeting viral N gene with normalization to HPRT for the indicated organs at 2, 4, and 6 dpi (left panel). Infectious virus titers detected by plaque assay in different organs at 2, 4, and 6 dpi (right panel). LOD=limit of detection. c. Lungs from uninfected (n=3), and infected (day 4 (n=4) and day 6 (n=3) p.i.) were analyzed by immunohistochemistry using anti-SARS-CoV-2 N antibody. d. Sections of paraffin-embedded lungs were stained with H&E. Note airway edema and alveolar hyaline membranes (asterisks, middle bottom panel), vascular thrombosis (inset, top right, 6 dpi 20x panel), dying cells with pyknotic to karyorrhectic nuclei, and a proliferative alveolar epithelium with mitotic figures (arrowhead and inset, lower right, 6 dpi 20x panel). e. Summary of histological scoring in the lungs, as described in Experimental Procedures.

Figure 2
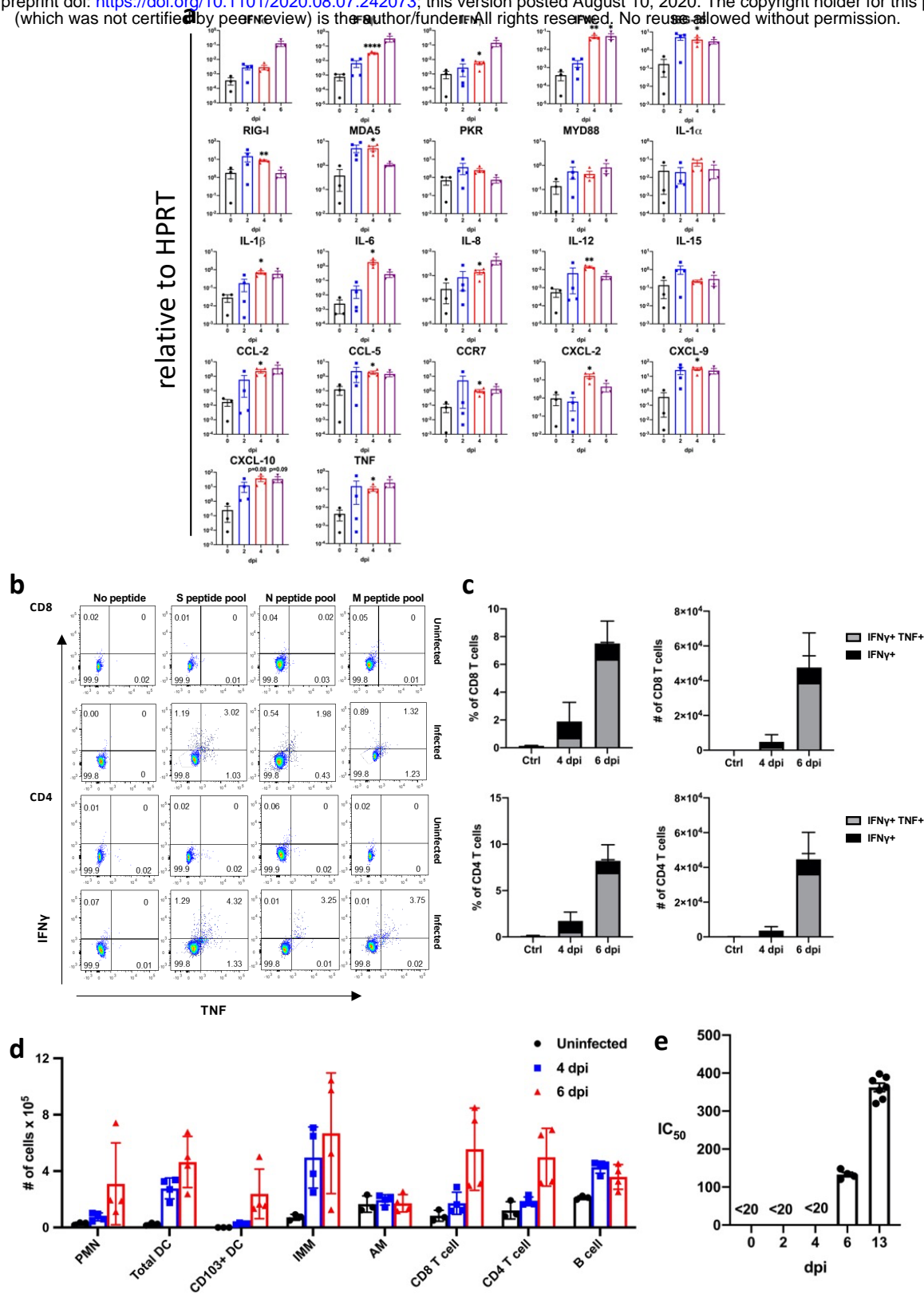
Fig. 2. Inflammatory mediators and immune effector cells contribute to lung disease phenotype. a. Cytokine and chemokine transcripts were measured by qPCR following reverse transcription of RNA isolated from the lungs of SARS-CoV-2 infected K18-hACE2 mice (n=3 or 4 for each time point). Statistical significance compared to results obtained at 0 dpi. b. Representative FACS plot of IFNγ+TNF+ CD8 and CD4 T cells after stimulated with indicated peptide pools) in the lungs of 10^5 PFU SARS-CoV-2 infected K18-hACE2 mice. c. Summary data are shown (n=3 mice/time point). d. Quantification of immune cells in the lungs (n=3 for uninfected group and n=4 for 4 and 6 dpi). e. Sera were collected from infected mice at the indicated time points and IC_{50} values determined by neutralization of SARS-CoV-2 pseudoviruses expressing luciferase.
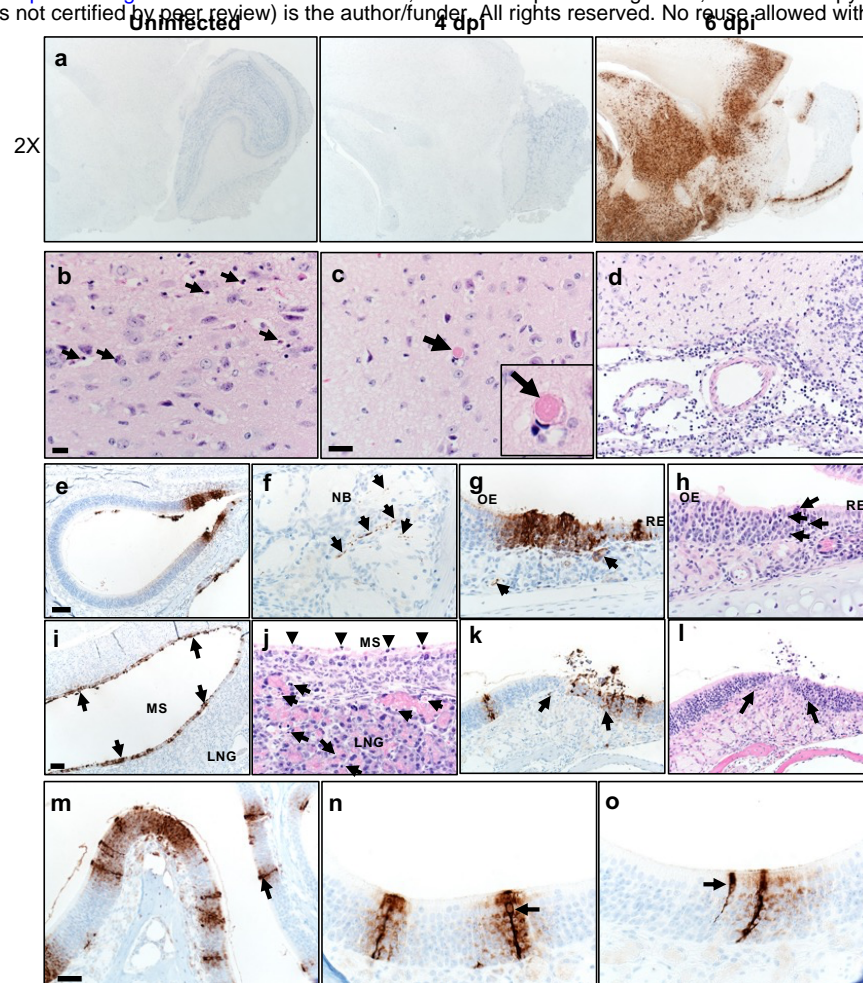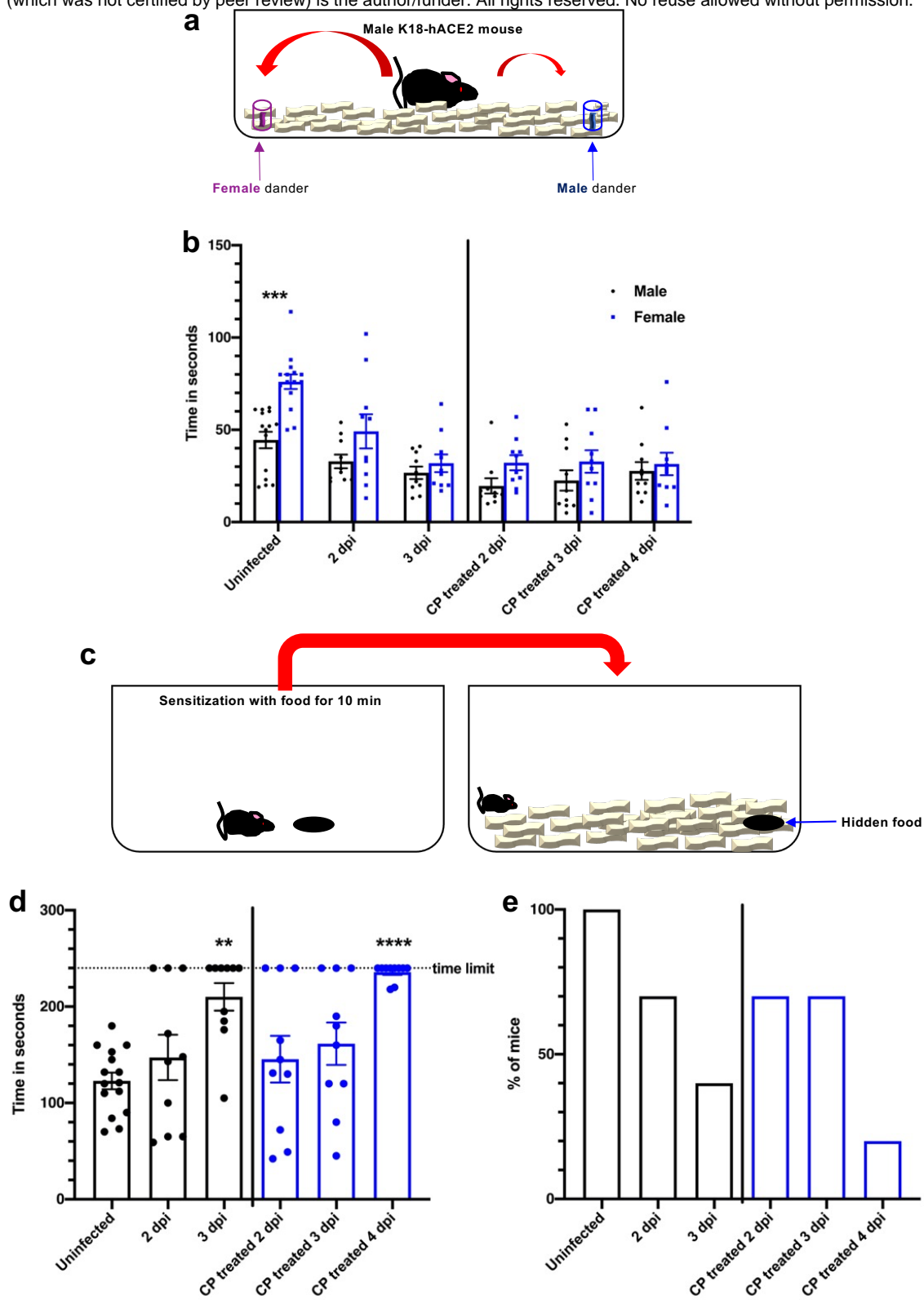
Figure 3

Fig. 3. Some K18-hACE2 mice develop brain disease after SARS-CoV-2 infection. a. Brains were prepared from uninfected and infected mice and analyzed for SARS-CoV-2 by immunohistochemistry. b, c. Multiple sites of dead cells (arrows) characterized by cellular and karyorrhectic nuclear debris (b, arrows) and of thrombi (c, arrow and inset) in thalamus. Bar = 17 μm. d. Examination of meninges at day 6 p.i. revealed increased cellularity composed of degenerate cells and neutrophils and mononuclear cells. Cellular and karyorrhectic nuclei debris were also detected in the perivascular regions (200X). e-o. Nasal and sinus tissue were examined at days 2 (e-j) and 5 (k-o) p.i. e-h. Olfactory epithelium (OE) was stained with anti-SARS-CoV-2 N antibody (e-g) or H&E stain (h). f. Nerve bundles (NB) subjacent to OE had punctate immunostaining (brown, arrows). g. Subjacent to sites of immunostaining for N protein (brown, black arrows), endothelial lining of vessels (left arrow) and bowman glands (right arrow) were occasionally positive for virus antigen (brown). h. Sites of N protein localization in OE had evidenced of cell death and cellular debris (arrows). Bar = 100 μm (e) and 25 μm (f-h). i-j. Maxillary sinus (MS) stained with anti-SARS-CoV-2 N antibody (i) or H&E (j). i. MS lining epithelium had extensive immunostaining for N protein (brown, arrows). j. ME epithelium had common sloughing and cellular debris (arrowheads). The lateral nasal glands (LNG) also had multifocal cellular and karyorrhectic debris (arrows). Bar = 75 μm (i) and 19 μm (j), respectively. k-l. Olfactory epithelium still had foci of SARS-CoV-2 N protein immunostaining at d. 5 p.i. (k, arrows, left) that was often localized near interface with respiratory epithelium. In these sites, there was cellular sloughing and loss of cellularity (arrows, right). 200x. m-o. Arrows point to "classic" morphology and strong labeling of sustentacular cells with expanding labeling of adjacent cells. Bar = 50 (m) and 25 μm (n, o).

Figure 4

Fig. 4. SARS-CoV-2 infection causes anosmia in K18-hACE2 mice.

a. Schematic showing social scent discrimination test. b. Each male mouse was allowed 5 minutes in the cage with male and female scent (bedding from male or female cages) placed at two corners of the cage. The time that male mice spent sniffing male or female scent was recorded. Data were analyzed by 2-way ANOVA. ***$p<0.001$. In some experiments, mice were pretreated with undiluted convalescent plasma (results on right of vertical line). c. Schematic showing buried food test. d. Buried food test. Food was buried under the bedding and each mouse was allowed 4 minutes in the cage to search for the food. The dotted line shows the time limit of 4 minutes. Data were analyzed by 1-way ANOVA. ****$p<0.0001$. e. The percentage of mice that found the buried food within 4 minutes is shown. In some experiments, mice were pretreated with undiluted convalescent plasma (denoted by blue bars in d, e).
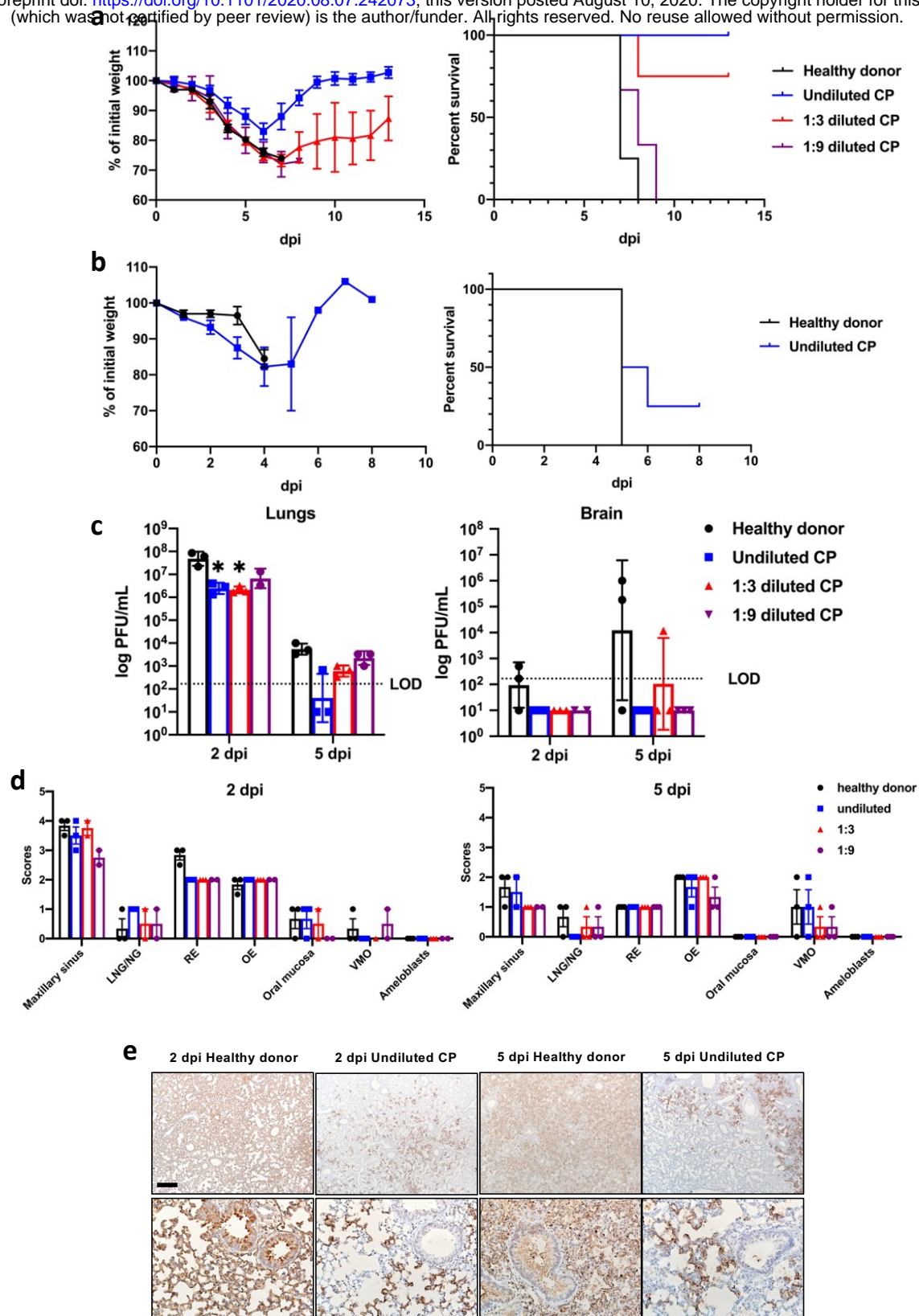
Figure 5

Fig. 5. Effects of convalescent plasma on outcomes in SARS-CoV-2-infected K18-hACE2 mice. a. Percentage of initial weight (left panel) and survival (right panel) of infected K18-hACE2 mice receiving control serum (n=4, black), undiluted (n=4, blue), 1:3 diluted (n=4, red) and 1:9 diluted (n=3, purple) human convalescent plasma at 24 hours prior to challenge of 10^5 PFU SARS-CoV-2. b. Percentage of initial weight (left panel), and survival (right panel) of K18-hACE2 mice receiving control plasma (n=2) or undiluted CP (n=4) at 24 hours after challenge with 10^5 PFU SARS-CoV-2. c. Viral titers of CP-treated mice in the lungs (left panel) and brains (right panel) at 2 and 5 dpi. LOD=limit of detection. d. Scoring for N protein abundance in CP-treated mice in the nasal cavity at 2 (left panel) and 5 (right panel) dpi. 0 – none; 1 - rare <1%; 2 - multifocal or localized <33% cells; 3 - multifocal, coalescing, 33-66%; 4 - extensive >67%. e. N protein staining in the lungs of control or convalescent plasma treated mice at 2 and 5 days p.i. Bar = 370 μm (top) and 75 μm (bottom).